# Electronic Supplementary Information

## Single-atom catalysts templated by metal-organic frameworks for electrochemical nitrogen reduction

Rui Zhang,†[a] Long Jiao,†[a] Weijie Yang,†[ab] Gang Wan [d] and Hai-Long Jiang *[ac]

[a] *Hefei National Laboratory for Physical Sciences at the Microscale, CAS Key Laboratory of Soft Matter Chemistry, Collaborative Innovation Center of Suzhou Nano Science and Technology, Department of Chemistry, University of Science and Technology of China, Hefei, Anhui 230026, P. R. China*

[b] *School of Energy and Power Engineering, North China Electric Power University, Baoding, Hebei 071003, P.R. China*

[c] *State Key Laboratory of Structural Chemistry, Fujian Institute of Research on the Structure of Matter, Fujian Institute of Innovation, Chinese Academy of Sciences, Fuzhou, Fujian 350002, P.R. China*

[d] *SSRL Materials Science Division, SLAC National Accelerator Laboratory and Stanford University, 2575 Sand Hill Road, Menlo Park, CA 94025, United States*

*† These authors contributed equally to this work.*

*To whom correspondence should be addressed.

E-mail: jianglab@ustc.edu.cn

## S1 Materials and Instrumentation

All of the reagents were commercially available and directly utilized: pyrrole (Energy Chemical, 99%), propanoic acid ($C_2H_5COOH$, Sinopharm Chemical Reagent Co., Ltd., AR), methyl 4-formylbenzoate (Energy Chemical, 98%), iron(II) chloride tetrahydrate ($FeCl_2 \cdot 4H_2O$, Sinopharm Chemical Reagent Co., Ltd., AR), cobalt(II) chloride hexahydrate ($CoCl_2 \cdot 6H_2O$, Sinopharm Chemical Reagent Co., Ltd., AR), nickel(II) chloride hexahydrate ($NiCl_2 \cdot 6H_2O$, Sinopharm Chemical Reagent Co., Ltd., AR), potassium hydroxide (KOH, Sinopharm Chemical Reagent Co., Ltd., AR), absolute ethanol ($C_2H_5OH$, Sinopharm Chemical Reagent Co., Ltd., AR), tetrahydrofuran (THF, Sinopharm Chemical Reagent Co., Ltd., AR), ethyl acetate ($CH_3COOEt$, Sinopharm Chemical Reagent Co., Ltd., AR), zirconyl chloride octahydrate ($ZrOCl_2 \cdot 8H_2O$, Aladdin Industrial Corporation, 98%), N,N-dimethylformamide (DMF, Sinopharm Chemical Reagent Co., Ltd., AR), acetone (Sinopharm Chemical Reagent Co., Ltd., AR), hydrofluoric acid (HF, Aladdin Industrial Corporation, 40%), trifluoroacetic acid ($CF_3COOH$, Energy Chemical, 99%), sodium hydroxide (NaOH, Sinopharm Chemical Reagent Co., Ltd., AR), ammonium chloride ($NH_4Cl$, Energy Chemical, 99.5%), salicylic acid (Aladdin Industrial Corporation, AR), sodium citrate (Sinopharm Chemical Reagent Co., Ltd., AR), sodium hypochlorite (NaClO, Sinopharm Chemical Reagent Co., Ltd., CP), sodium nitroferricyanide dehydrate (Aladdin Industrial Corporation, AR), 4-dimethylaminobenzaldehyde (Energy Chemical, 99%), ammonium chloride with the $^{15}N$ enrichment of 99% (Aladdin Industrial Corporation, 98%), 117 Nafion membrane (Dupont), de-ionized water (18.25 MΩ·cm, Cleaned

Water Treatment Co., Ltd., Hefei).

Powder X-ray diffraction patterns (PXRD) were acquired on a Japan Rigaku SmartLab$^{TM}$ rotation anode X-ray diffractometer equipped with graphite monochromatized Cu Kα radiation (λ = 1.54 Å). UV-Vis spectra were performed on a UV-Vis spectrometer (UV-2700 Shimadzu). Field-emission scanning electron microscopy (FE-SEM) images were acquired on the Zeiss Supra 40 scanning electron microscope operated at 5 kV. The transmission electron microscopy (TEM) images were obtained on JEOL-2010 instrument operated at 200 kV. High-angle annular dark-field scanning transmission electron microscopy (HAADF-STEM) was measured on JEOL ARM-200F with an electron acceleration energy of 200 kV. Nitrogen sorption was measured on Micromeritics ASAP 2020 system at 77 K. The inductively coupled plasma atomic emission spectroscopy (ICP-AES) and elemental analysis were operated on Optima 7300 DV and Elementar vario EL cube analyzer, respectively. X-ray photoelectron spectroscopy (XPS) experiment was operated on ESCALAB 250 spectrometer with monochromatized Al Kα excitation source ($hv$ = 1486.7 eV). In the NRR test, $N_2$ (99.9999%, Nanjing Shangyuan) was purged with a rate of 40 sccm, which was strictly monitored by mass flowmeter (Beijing Sevenstar Electronics Co., Ltd.).

The X-ray absorption spectra were recorded at 1W1B beamline of Beijing Synchrotron Radiation Facility (BSRF) at 2.5 GeV. Fe foil, Co foil, Ni foil, $Fe_2O_3$, CoO and $Ni_2O_3$ were utilized as the references. By utilizing Si (111) double-crystal monochromator, the data were acquired in the fluorescence mode under ambient

conditions. The data analyses were carried out with the Athena and Artemiss software packages.

## S2 Experimental Section

### 2.1 The determination of ammonia contamination in the control experiments.

The control experiments were performed according to the protocols in the literature.[S1]

#### 2.1.1 The determination of ammonia contamination in the blank electrolyte.

The ammonia contamination of the blank electrolyte (0.1 M HCl) is determined by the indophenol blue method and the result indicates that the ammonia concentration is below the limit of detection (LOD).

#### 2.1.2 The determination of ammonia contamination in the acid trap solution.

The ammonia contamination of the acid solution (0.05 M $H_2SO_4$) in the trap is determined by the indophenol blue method and the result indicates that the ammonia concentration is below the LOD.

#### 2.1.3 The determination of ammonia contamination in the electrocatalytic system.

The electrocatalytic tests were performed under Ar (99.9999%, Nanjing Shangyuan) atmosphere at open-circuit voltage in 0.1 M HCl on the $Fe_1$-N-C electrode. Then the electrolyte was taken out and the ammonia concentration is determined by the indophenol blue method. The result indicates that the ammonia concentration is 0.01 μg/mL. Furthermore, the electrocatalytic tests were also carried out under Ar atmosphere at -0.05 V vs RHE in 0.1 M HCl on the $Fe_1$-N-C electrode, with the ammonia concentration of 0.01 μg/mL. It is worth noting that the ammonia contamination under Ar atmosphere should be subtracted from the reported NRR ammonia yields.

#### 2.1.4 The determination of ammonia contamination in the supplied $N_2$.

The ammonia and $NO_X$ contamination of the supplied $N_2$ is determined by the flow injection analysis (FIA) method and the result indicates that the contaminant concentration is below the LOD.

**2.1.5 The determination of ammonia contamination on the pure carbon paper electrode.**

The electrocatalytic test was carried out under $N_2$ atmosphere at -0.05 V vs RHE in 0.1 M HCl on the pure carbon paper electrode and the result indicates that the ammonia concentration is below the LOD.

**2.2 $^{15}N_2$ isotope labeling experiments.**

The isotopic labeling experiment was carried out using $^{15}N_2$ as the feeding gas (Wuhan NEWRADAR SPECIAL GAS CO., LTD., Purity 99%). Before the experiments, the ammonia and $NO_X$ contamination of the supplied $^{15}N_2$ is determined following the procedures mentioned in 2.1.4. The result indicates that the contaminant concentration is below the LOD and thus cannot affect the calculation of the $^{15}NH_3$ amount during NRR. The $^{15}N_2$ applied in isotope labeling underwent purification by passing through the acid trap containing 0.05 M $H_2SO_4$. The electrolyte was bubbled with $^{15}N_2$ at 10 sccm for 30 min to saturate the electrocatalytic system. The electrolysis was conducted at -0.05 V vs. RHE for 2 h, with the continuous $^{15}N_2$ bubbling at 40 sccm.

**S3. Computational studies.**

The Perdew-Burke-Ernzerhof (PBE) functional, as well as the projector augmented wave (PAW) potentials were selected to accomplish the DFT calculations, which is proven appropriate for graphene-based material. The calculations were performed with the VASP 5.4.1 program. Considering the magnetic effect, the spin polarization correction was taken into account. Consistent with previous studies, in order to simulate the catalyst surface, a 4×4 graphene with vacuum layer of 15 Å was adopted.[S2,S3] As for the accurate electronic energy in ground-state, a Γ-centered 15×15×1 k-point was utilized and the cutoff energy was 500 eV. The convergence standards of energy and force were selected as $10^{-5}$ eV and 0.02 eV/Å. The vibrational frequency with finite displacements of ± 0.02 Å was taken into account to obtain the zero point energy correction and vibrational entropy correction.

The variation of Gibbs free energy for each step (ΔG) along $N_2$ reduction reaction pathway was calculated through the standard hydrogen electrode (SHE) model.[S4] According to this calculation model, ΔG can be calculated as follows:

$$\Delta G = \Delta E + \Delta ZPE - T\Delta S + \Delta G_U + \Delta G_{pH} \quad (1)$$

where ΔE is the difference of electronic energy in ground-state acquired from self-consistent calculation; ΔZPE is the difference of zero point energy; T is the temperature (T=298.15 K); ΔS is the difference of entropy; $\Delta G_U$ is the donation of applied electrode potential to Gibbs free energy; $\Delta G_{pH}$ is the is the contribution of $H^+$ concentration to Gibbs free energy, which is calculated from $\Delta G_{pH} = 2.303 \times k_B T \times pH$ (pH=0, $\Delta G_{pH}$=0). The entropies as well as the vibrationa frequencies of molecules in the gas phase were in accordance with the NIST database.[S5]

As for the DFT calculations of NRR, we fully considered the possible mechanism including dissociative mechanism and associative mechanism. Due to the high energy for the cleavage of N-N triple bond in the dissociative mechanism, it was ruled out firstly. Therefore, we mainly focused on the traditionally considered distal and alternating pathways in associative mechanism.

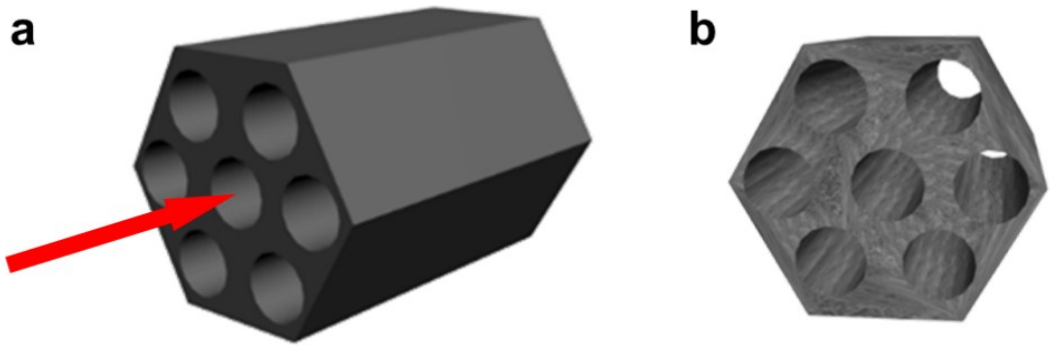


**Scheme S1** (a) The three-dimensional perspective of $Fe_1$-N-C featuring rod-shaped morphology. The red arrow stands for the axial direction. (b) The view from the axial direction, which is also depicted in Scheme 1. The honeycomb-like structure represents the 1D open channels.

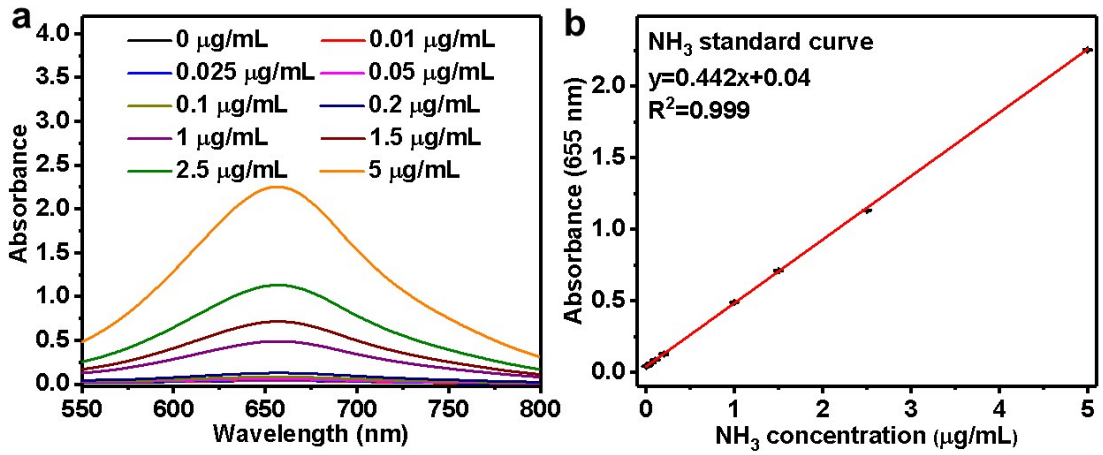


**Fig. S1** (a) UV-Vis spectra and (b) concentration-absorbance curve of $NH_3$ with a series of standard concentration ranging from 0 to 5 μg/mL.

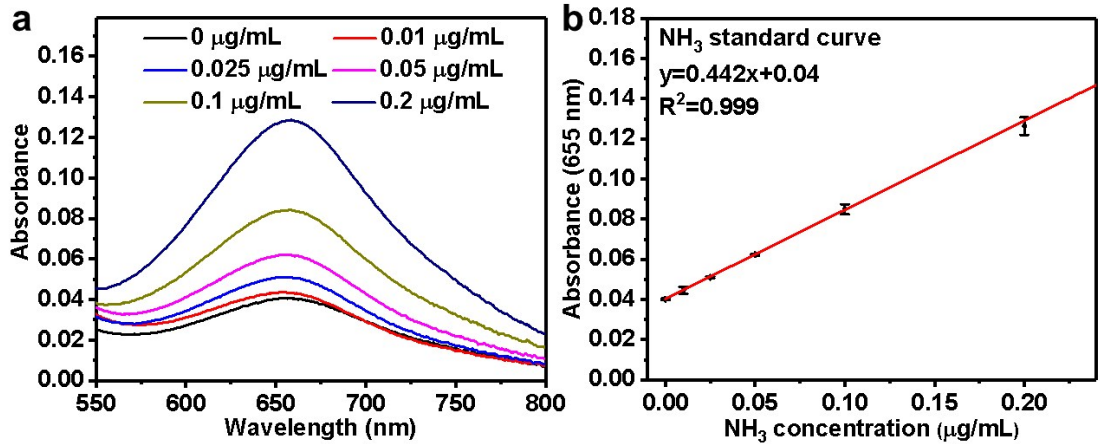


**Fig. S2** (a) UV-Vis spectra and (b) concentration-absorbance curve of $NH_3$ with a series of standard concentration in the range where ammonia was synthesized in this work, ranging from 0 to 0.2 μg/mL.

**The calculation of the limit of detection (LOD) of the indophenol blue method:**

The absorbance of the blank sample ($X_{Bj}$, j=1 to 20) has been tested for 20 times and the values are as follows: 0.0392, 0.0407, 0.0397, 0.0392, 0.0398, 0.0390, 0.0400, 0.0408, 0.0411, 0.0401, 0.0400, 0.0406, 0.0412, 0.0400, 0.0395, 0.0399, 0.0402,

0.0408, 0.0396, 0.0401. The mean value of the blank responses ($X_B$) can be calculated as

$$\bar{X}_B = \frac{\sum_{j=1}^{20} X_{Bj}}{20} = 0.0401$$

According to the equation of the calibration curve (y=0.442x + 0.04), the mean concentration of the blank samples, $\bar{C}_B$, can be calculated as $1.7 \times 10^{-4}$ μg/mL.

The standard deviation, $S_B$, can be calculated as

$$S_B = \sqrt{\frac{\sum_{j=1}^{20} (C_{Bj} - \bar{C}_B)^2}{20 - 1}} = 0.0014$$

In defining LOD, i. e. $C_L$, IUPAC states that [S6]

$$C_L = \frac{k S_B}{m} = \frac{3 \times 0.0014}{0.442} = 0.0095 \text{ μg/mL}$$

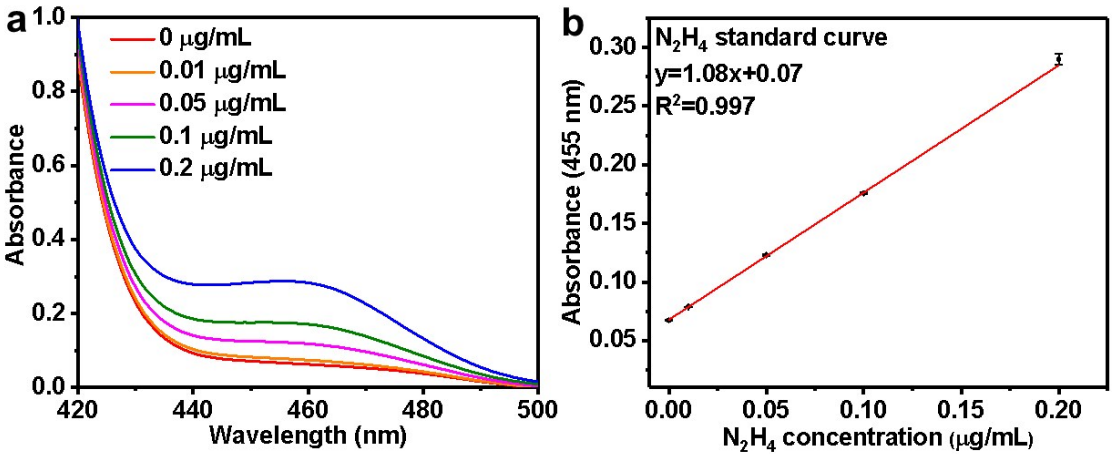


**Fig. S3** (a) UV-Vis spectra and (b) concentration-absorbance curve of $N_2H_4$ with a series of standard concentration.

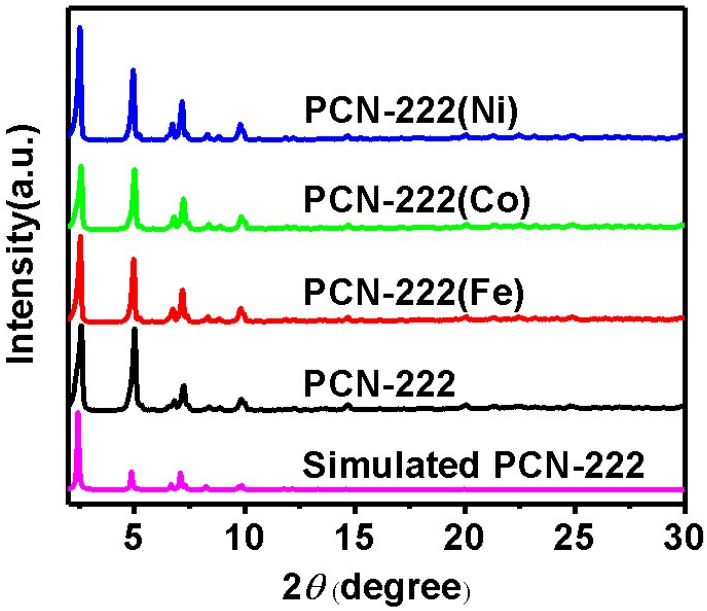


**Fig. S4** Powder XRD results of PCN-222, PCN-222(Fe), PCN-222(Co), PCN-222(Ni) and simulated PCN-222.

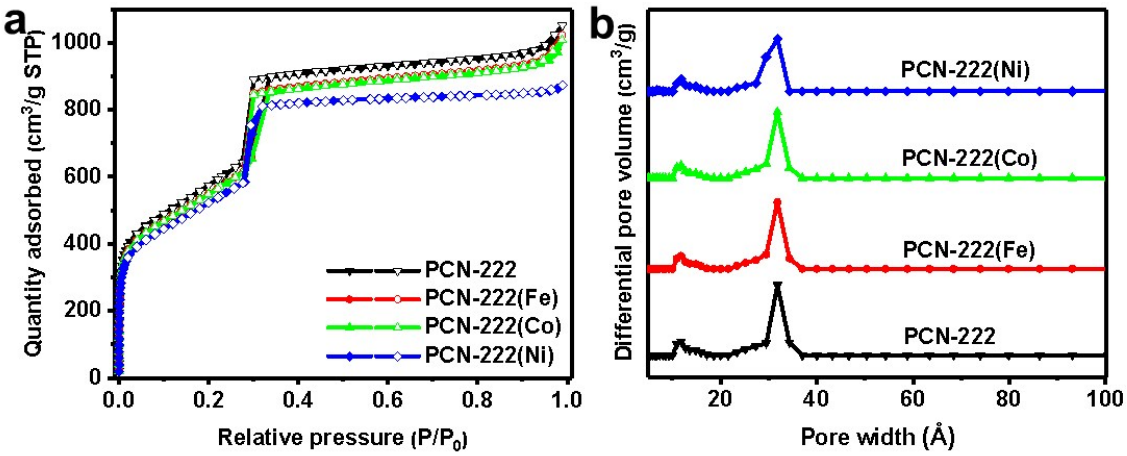


**Fig. S5** (a) $N_2$ sorption isotherms at 77 K and (b) the respective pore size distributions for PCN-222, PCN-222(Fe), PCN-222(Co) and PCN-222(Ni).

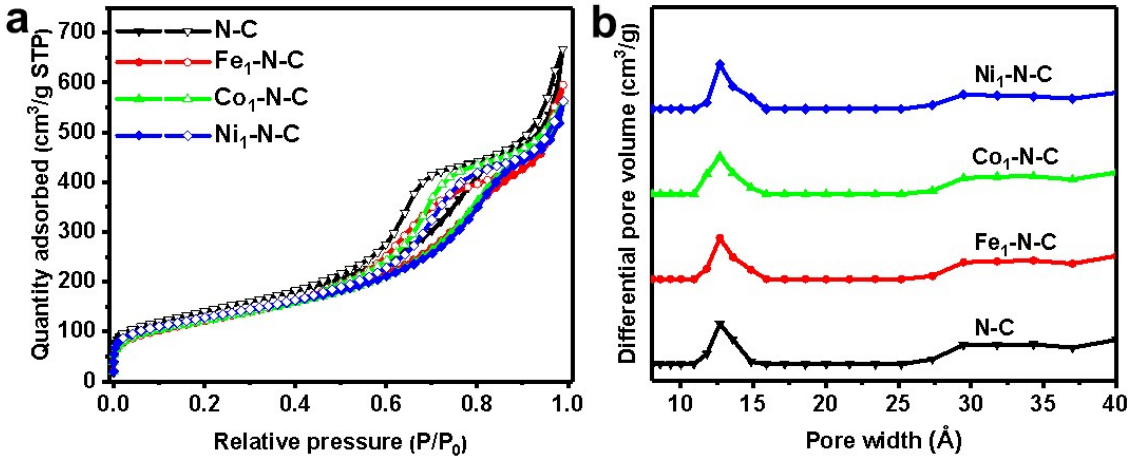


**Fig. S6** (a) $N_2$ sorption isotherms at 77 K and (b) the respective pore size distributions for N-C, $Fe_1$-N-C, $Co_1$-N-C and $Ni_1$-N-C.

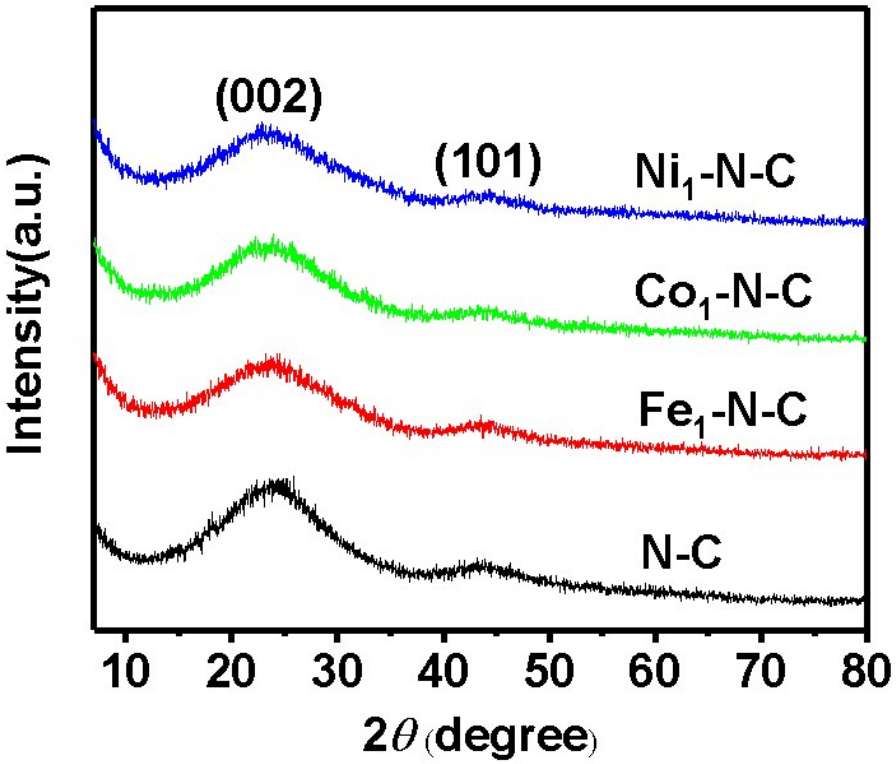


**Fig. S7** Powder XRD patterns of N-C, $Fe_1$-N-C, $Co_1$-N-C and $Ni_1$-N-C.

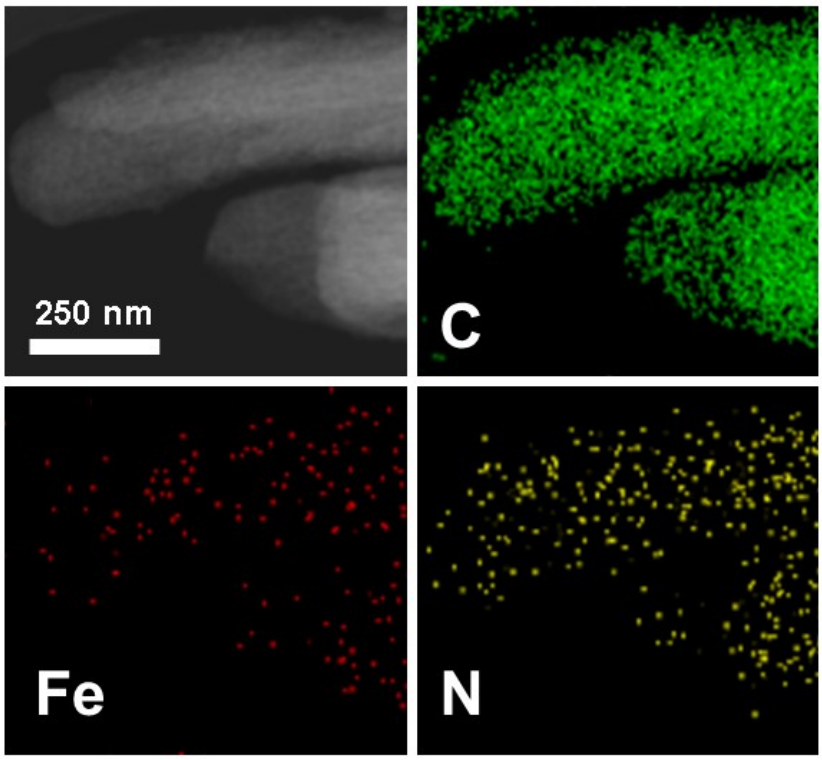


**Fig. S8** EDS mapping of $Fe_1$-N-C.

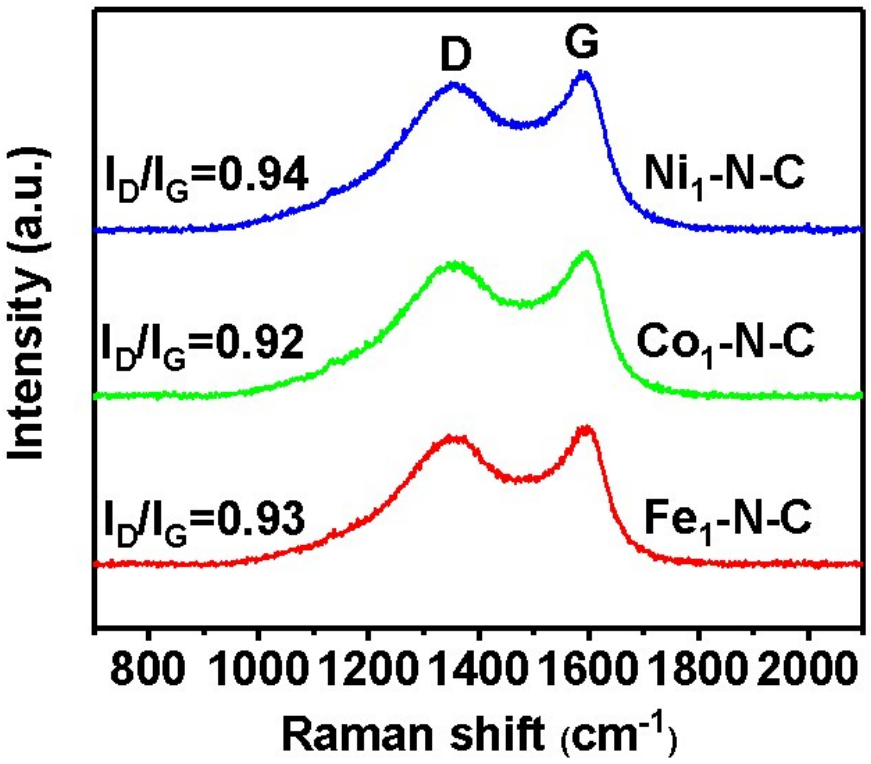


**Fig. S9** Raman spectra of $Fe_1$-N-C, $Co_1$-N-C and $Ni_1$-N-C.

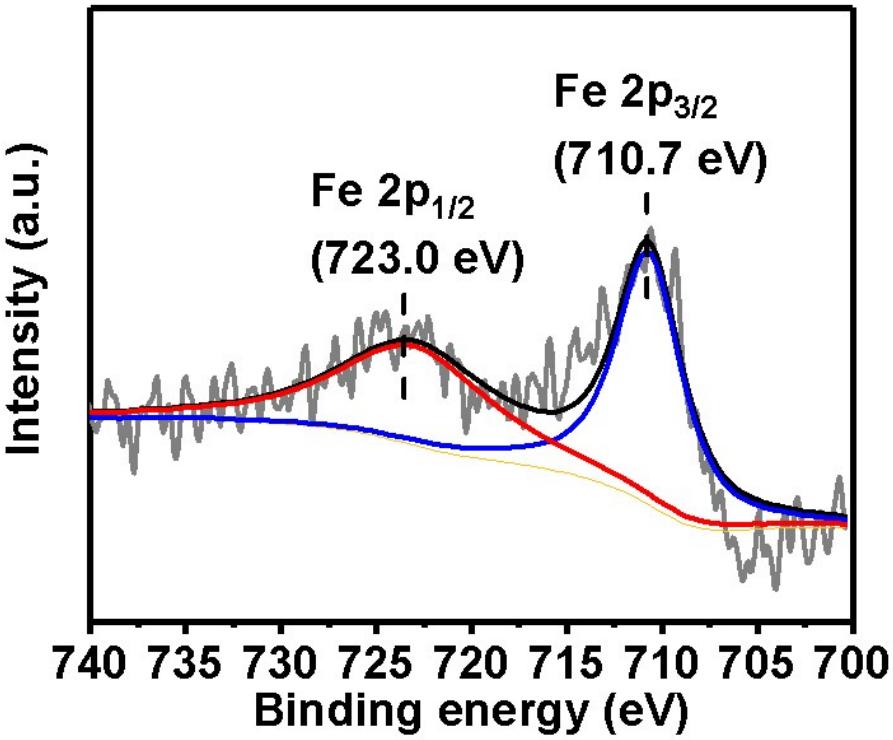


**Fig. S10** XPS spectrum for the Fe 2p region of $Fe_1$-N-C.

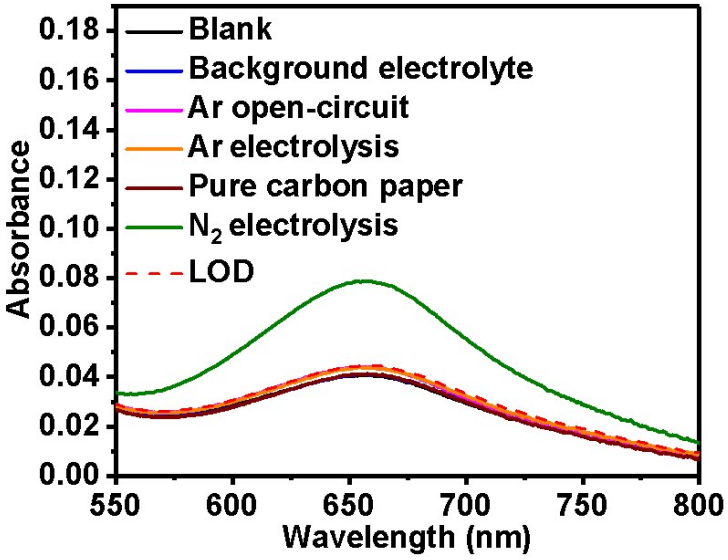


**Fig. S11** UV-Vis absorption spectra comparison between the samples of the control experiments and the NRR of $Fe_1$-N-C at -0.05 V.

The above results indicate that the background electrolyte does not contain the contaminants including ammonia or $NO_x$. The Ar control experiments were conducted

in both the open-circuit and electrocatalytic conditions at -0.05 V for 2 h, with the ammonia concentration of 0.01 μg/mL, which was subtracted from the reported NRR ammonia yields. When NRR proceeded on the pure carbon paper, the concentration of ammonia or $NO_x$ is below the limit of detection (LOD), indicating that the pure carbon paper does not show the NRR activity. The NRR of $Fe_1$-N-C at -0.05 V exhibits the highest concentration of ammonia and the absorbance lies above the LOD, which is clearly distinct from the samples of the control experiments.

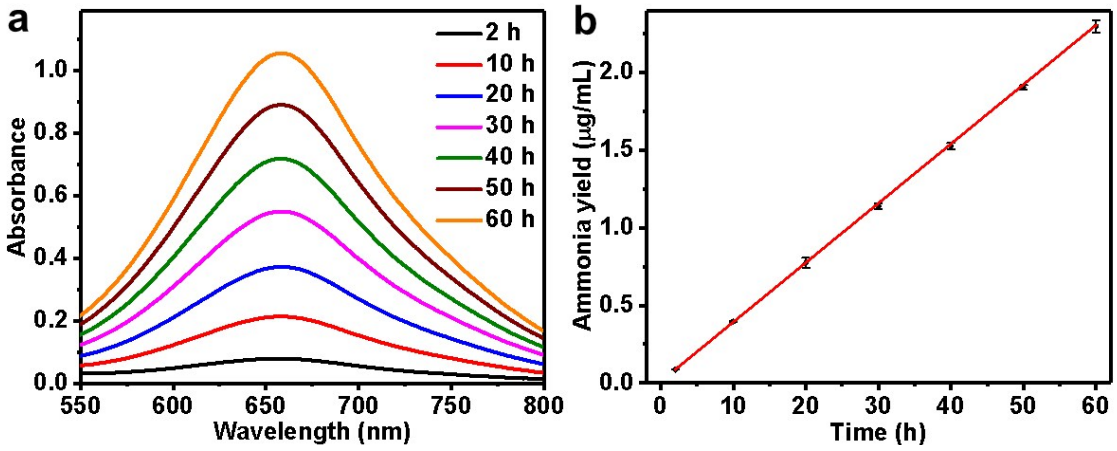


**Fig. S12** (a) UV-Vis absorption spectra of the time dependent NRR for $Fe_1$-N-C at -0.05 V, (b) The corresponding ammonia yield.

As for the calculation of turnover number (TON), $TON=n_{prod.}/n_{cat.}$, where the amount of the produced ammonia ($n_{prod.}$) is calculated according to the results from indophenol blue method, and the amount of the catalyst ($n_{cat.}$) is attributed to the loading amount of Fe.

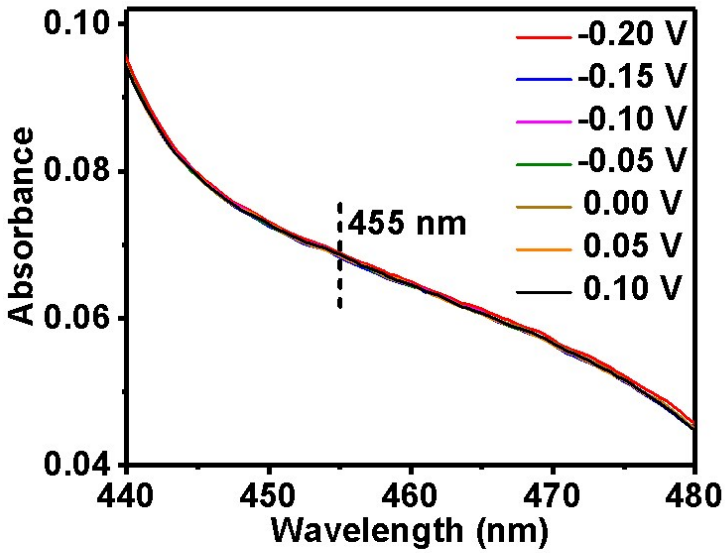


**Fig. S13** UV-Vis spectra of the electrolyte for the determination of $N_2H_4$ at various potentials on $Fe_1$-N-C.

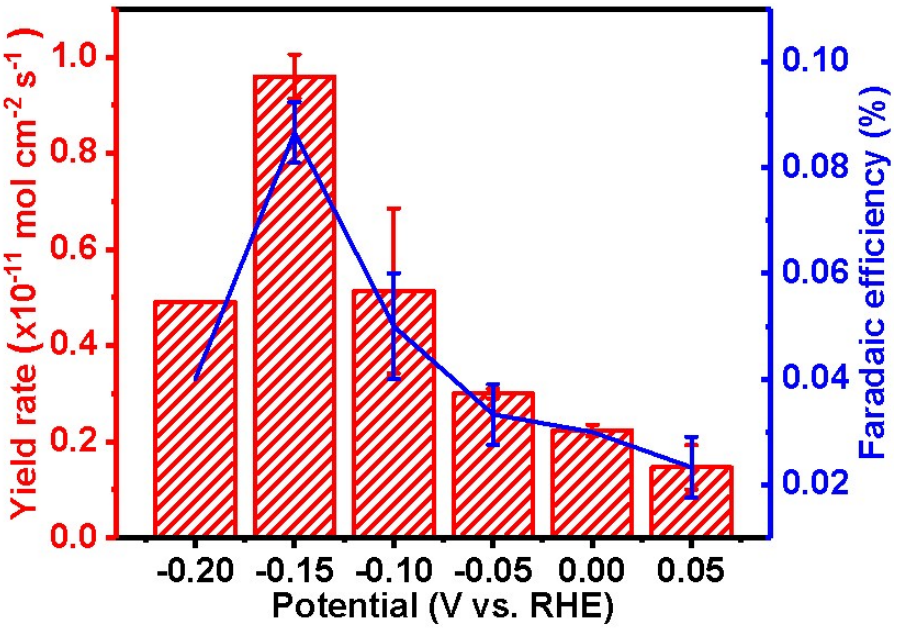


**Fig. S14** (a) $NH_3$ yield rate and (b) FE of N-C at various potentials.

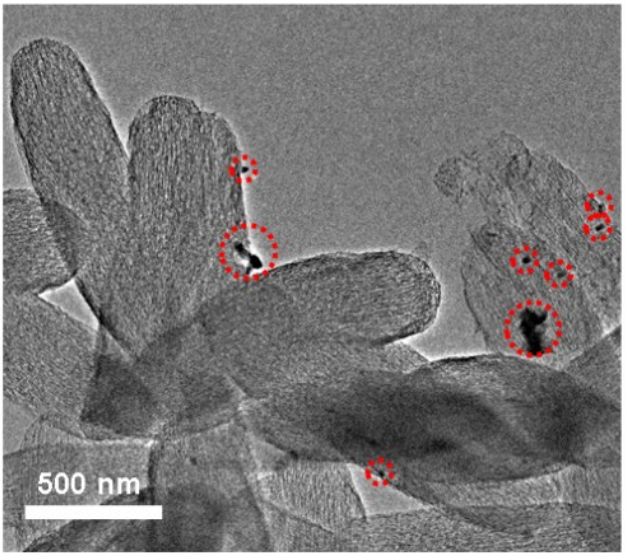


**Fig. S15** TEM image of $Fe_{NP}$-N-C.

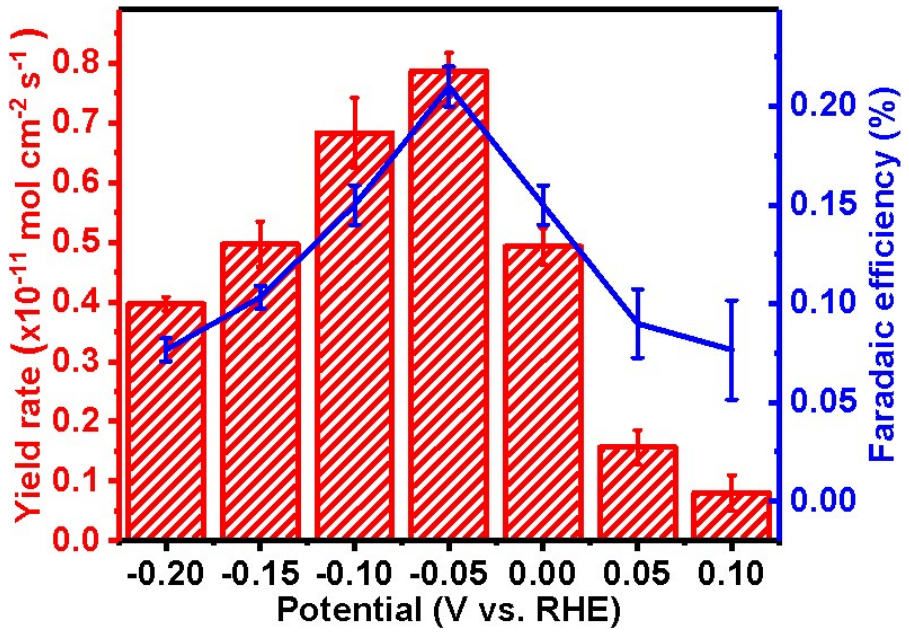


**Fig. S16** (a) $NH_3$ yield rate and (b) FE of $Fe_{NP}$-N-C at various potentials.

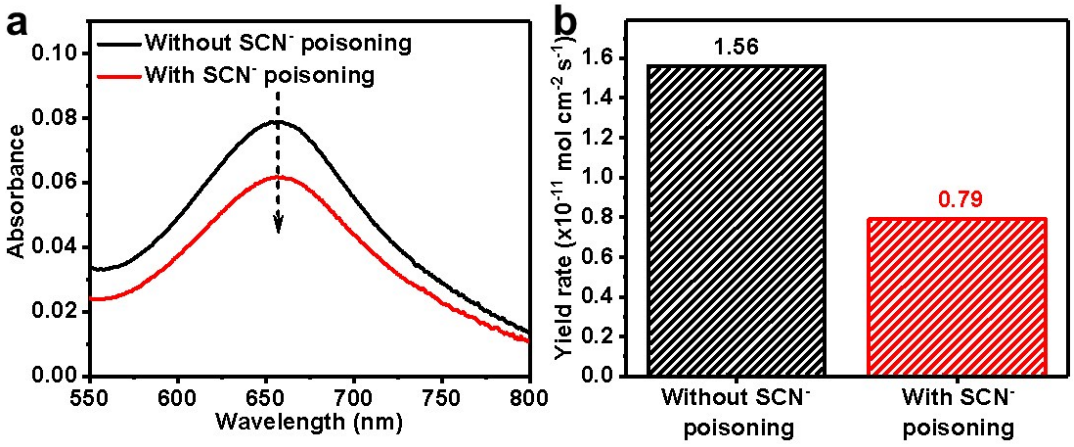


**Fig. S17** (a) The comparison of the UV-Vis absorption spectra of the NRR for $Fe_1$-N-C at -0.05 V between the sample with 0.01 M KSCN poisoning and the sample without KSCN poisoning. (b) The corresponding $NH_3$ yield rates.

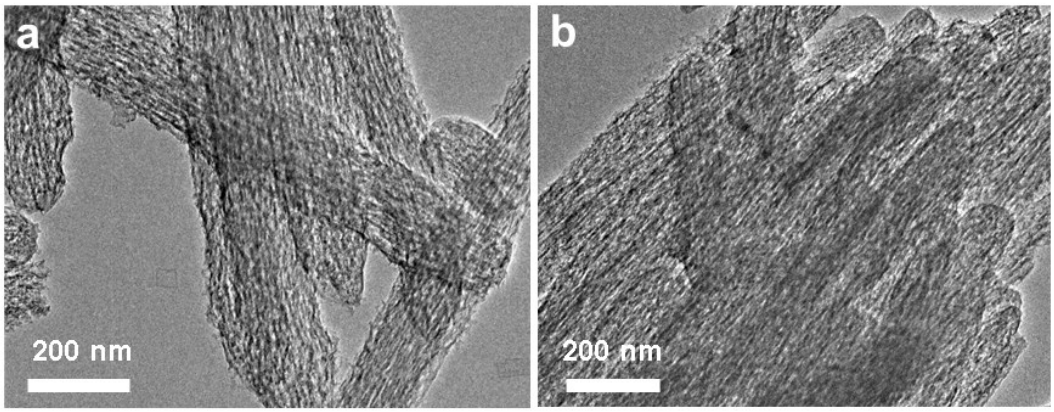


**Fig. S18** (a) TEM images of $Co_1$-N-C and (b) $Ni_1$-N-C.

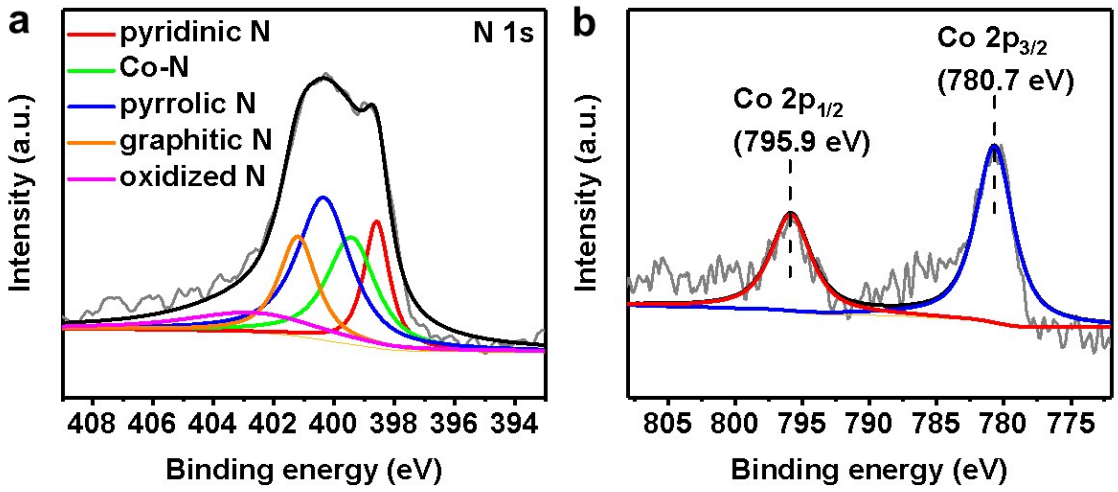


**Fig. S19** (a) XPS spectra for the N 1s region and (b) Co 2p region of $Co_1$-N-C.

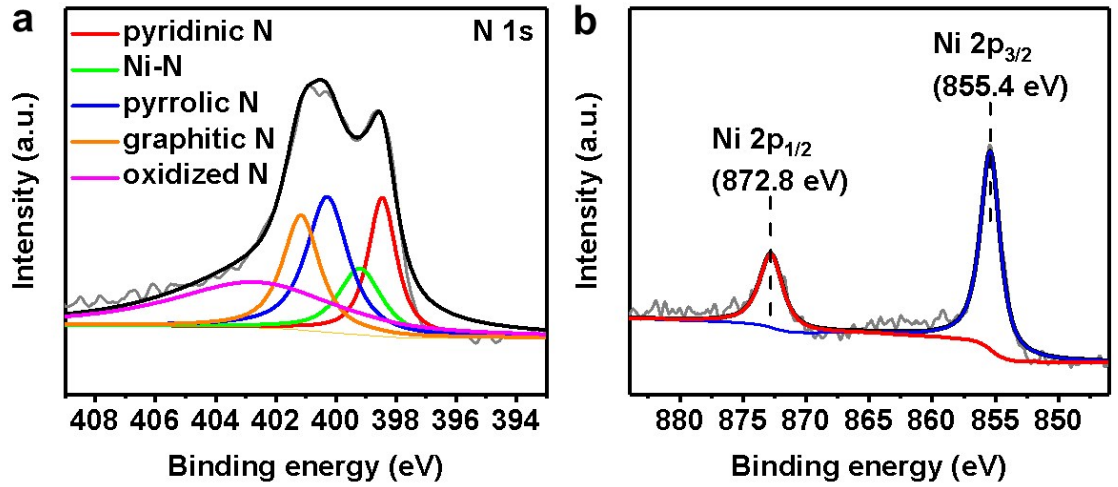


**Fig. S20** (a) XPS spectra for the N 1s region and (b) Ni 2p region of $Ni_1$-N-C.

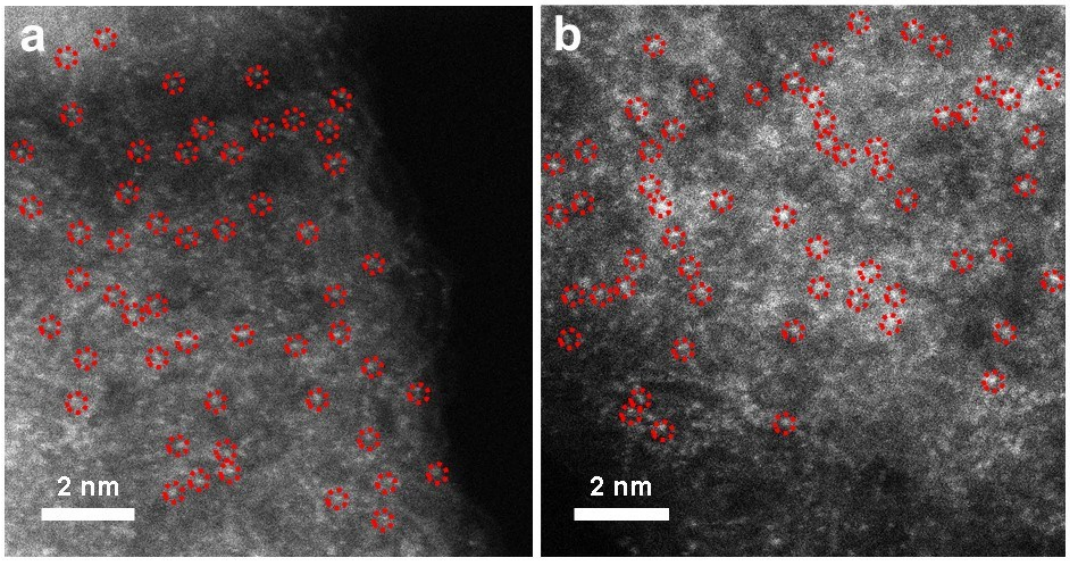


**Fig. S21** Aberration-corrected HAADF-STEM images of (a) $Co_1$-N-C and (b) $Ni_1$-N-C.

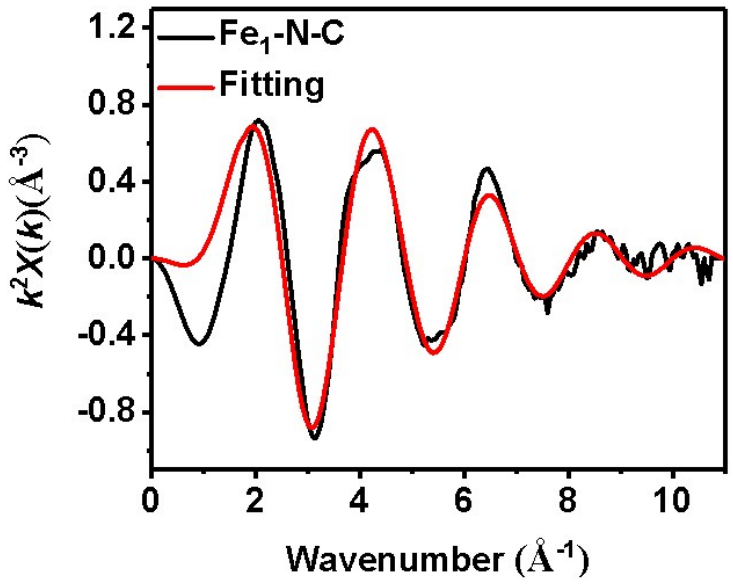


**Fig. S22** EXAFS k-space fitting results of $Fe_1$-N-C.

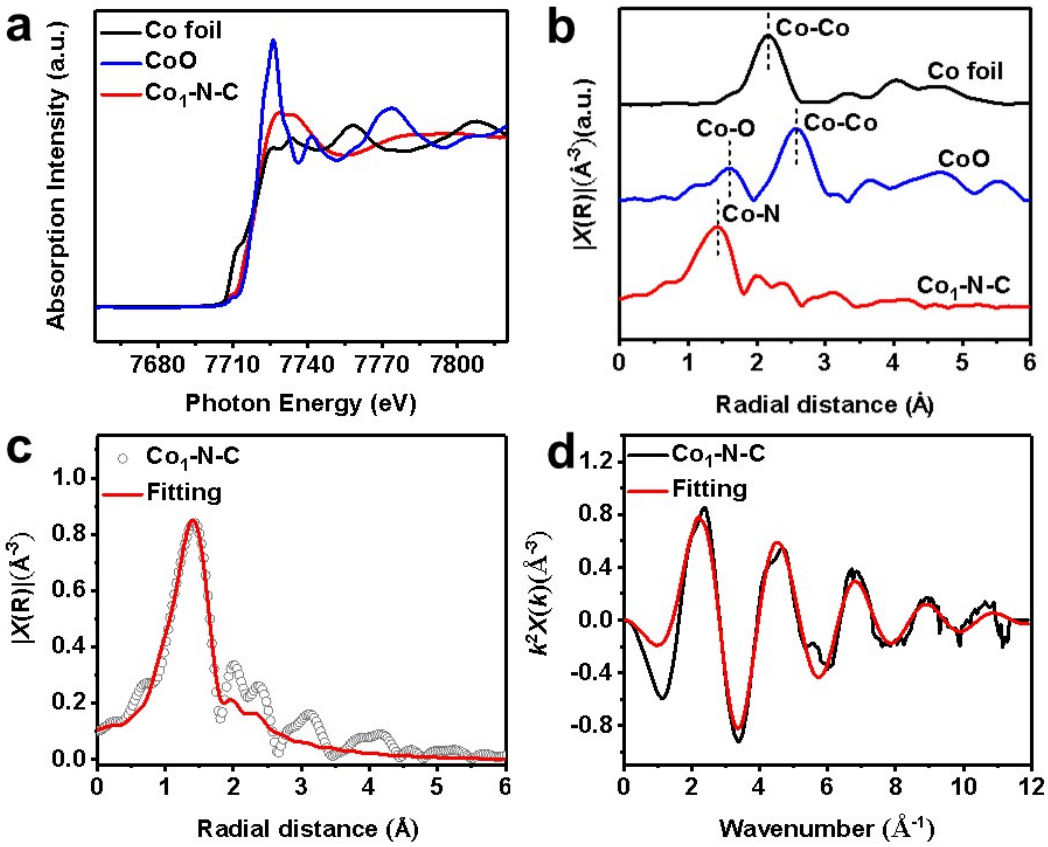


**Fig. S23** (a) Co K-edge XANES and (b) FT-EXAFS spectra of $Co_1$-N-C, CoO and Co foil. (c) EXAFS fitting curve and (d) EXAFS k-space fitting results of $Co_1$-N-C.

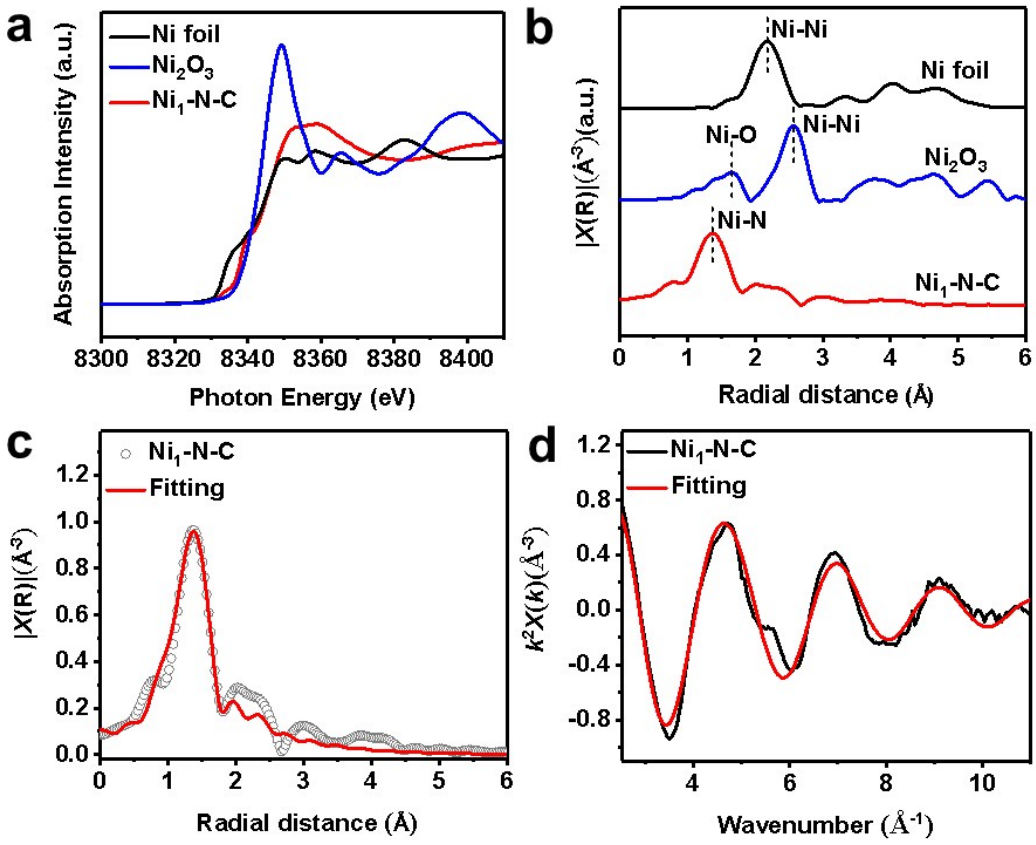


**Fig. S24** (a) Ni K-edge XANES and (b) FT-EXAFS spectra of $Ni_1$-N-C, $Ni_2O_3$ and Ni foil. (c) EXAFS fitting curve and (d) EXAFS k-space fitting results of $Ni_1$-N-C.

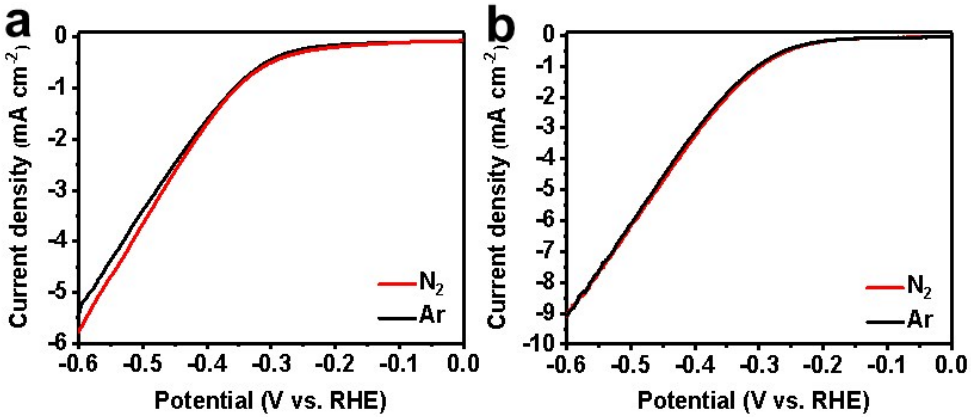


**Fig. S25** (a) LSV curves of $Co_1$-N-C in $N_2$ and Ar-saturated 0.1 M HCl measured at 5 mV/s. (b) LSV curves of $Ni_1$-N-C in $N_2$ and Ar-saturated 0.1 M HCl measured at 5 mV/s.

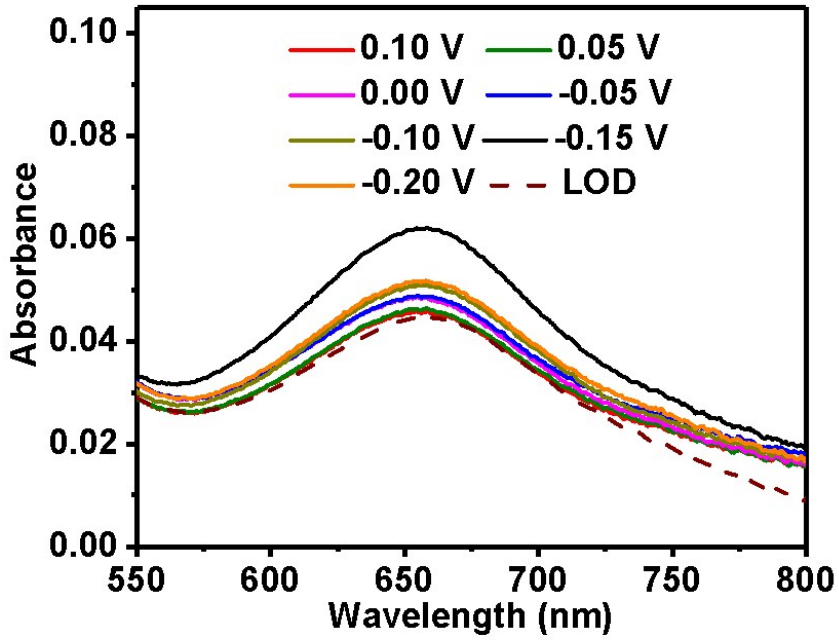


**Fig. S26** UV-Vis spectra of the electrolyte at various potentials on $Co_1$-N-C.

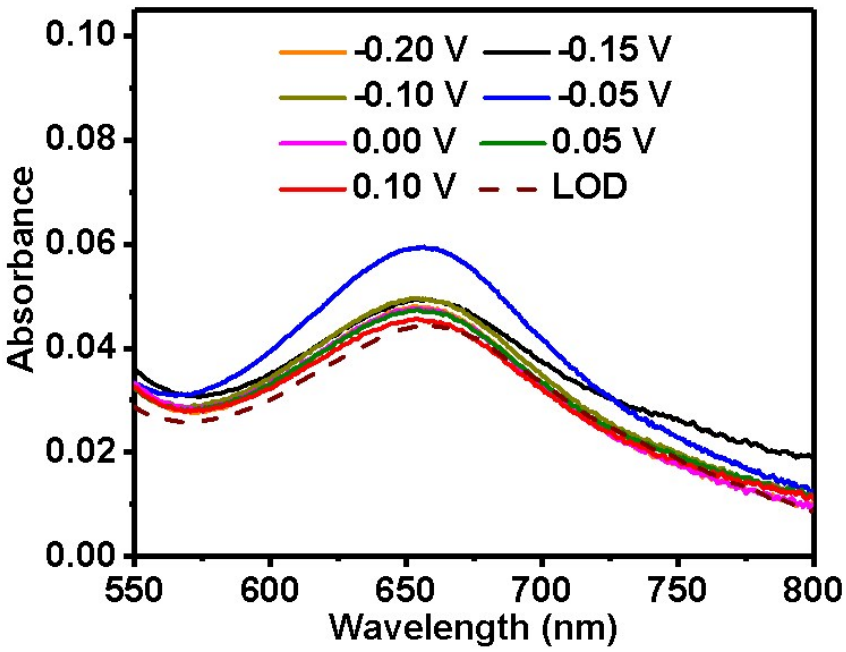


**Fig. S27** UV-Vis spectra of the electrolyte at various potentials on $Ni_1$-N-C.

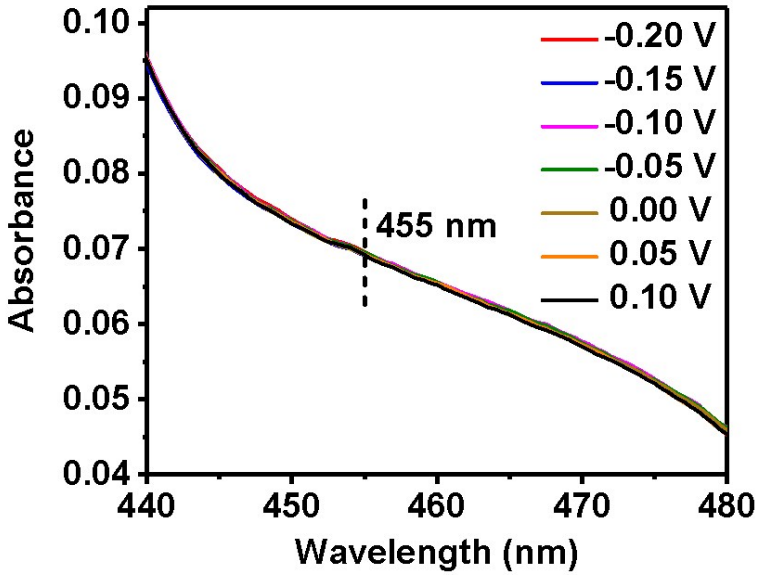


**Fig. S28** UV-Vis spectra of the electrolyte for the determination of $N_2H_4$ at various potentials on $Co_1$-N-C.

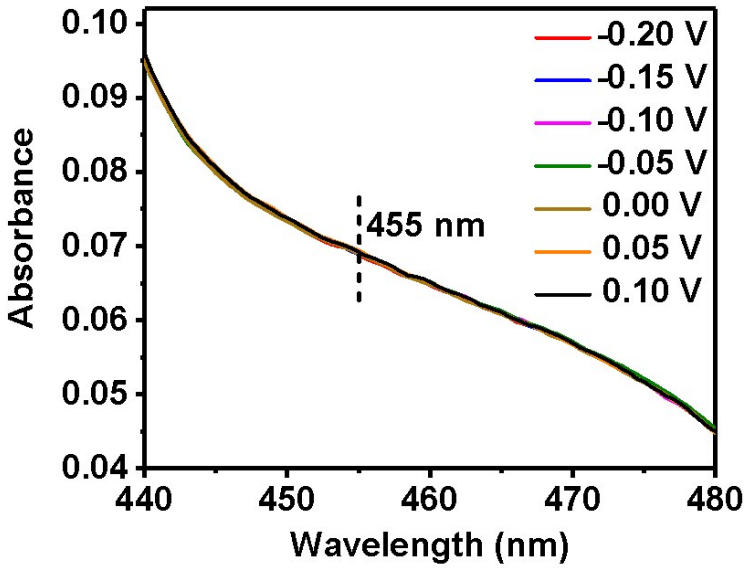


**Fig. S29** UV-Vis spectra of the electrolyte for the determination of $N_2H_4$ at various potentials on $Ni_1$-N-C.

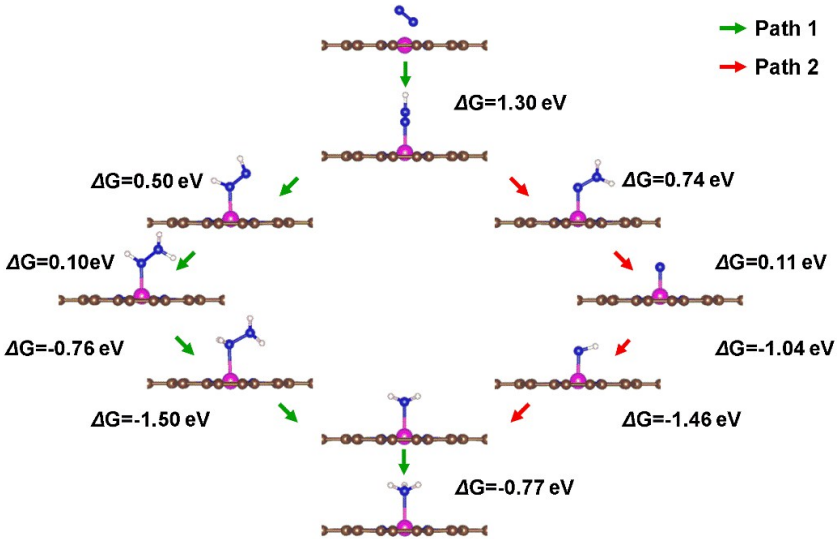


**Fig. S30** The reaction diagram of NRR on the surface of $Co_1$-N-C.

According to the ΔG, the NRR on $Co_1$-N-C favors path 1 (the alternating pathway), which has lower energy barrier for the RDS than that of path 2 (the distal pathway).

**Table S1** The ICP-AES data of $Fe_1$-N-C, $Co_1$-N-C and $Ni_1$-N-C.

| Catalysts | $Fe_1$-N-C | $Co_1$-N-C | $Ni_1$-N-C |
|---|---|---|---|
| Metal Content (wt%) | 1.71 | 1.68 | 1.76 |

**Table S2** The N content of $Fe_1$-N-C determined by XPS and elemental analysis.

| Method | XPS | Elemental analysis |
|---|---|---|
| N Content | 4.15 (at%) | 4.81 (wt%) |

The N content determined by XPS, 4.15 (at%), can be converted to 4.78 (wt%). Besides, considering that XPS only reflects the information of the catalyst surface, elemental analysis has also been performed and the N content is 4.81% (wt%), which is consistent with the result obtained by XPS.

**Table S3** Parameters of the best Fe K-edge EXAFS fitting results for $Fe_1$-N-C.

| **Catalysts** | **shell** | **CN** | **R (Å)** | **$\sigma^2$ ($10^{-3}$Å$^2$)** | **$\Delta$E (eV)** | **R factor** | ***K*-Range (Å$^{-1}$)** | **R-Range (Å)** |
|---|---|---|---|---|---|---|---|---|
| **$Fe_1$-N-C** | **Fe-N** | **3.51** | **1.96** | **9.97** | **-6.579** | **0.0061** | **2.5 - 10.5** | **1.03 -2.1** |

**Table S4** The N content of $Co_1$-N-C determined by XPS and elemental analysis.

| Method | XPS | Elemental analysis |
|---|---|---|
| N Content | 4.31 (at%) | 4.98 (wt%) |

The N content determined by XPS, 4.31 (at%), can be converted to 4.93 (wt%). Besides, considering that XPS only reflects the information of the catalyst surface, elemental analysis has also been performed and the N content is 4.98% (wt%), which is consistent with the result obtained by XPS.

**Table S5** The N content of $Ni_1$-N-C determined by XPS and elemental analysis.

| Method | XPS | Elemental analysis |
|---|---|---|
| N Content | 4.08 (at%) | 4.75 (wt%) |

The N content determined by XPS, 4.08 (at%), can be converted to 4.67 (wt%). Besides, considering that XPS only reflects the information of the catalyst surface, elemental analysis has also been performed and the N content is 4.75% (wt%), which is consistent with the result obtained by XPS.

**Table S6** Parameters of the best Co K-edge EXAFS fitting results for $Co_1$-N-C.

| Catalysts | shell | CN | R (Å) | $\sigma^2$ ($10^{-3}$Å$^2$) | ΔE (eV) | R factor | *K*-Range (Å$^{-1}$) | R-Range (Å) |
|---|---|---|---|---|---|---|---|---|
| **$Co_1$-N-C** | **Co-N** | **3.9** | **1.89** | **8.62** | **-2.515** | **0.003** | **2.5 – 11.3** | **1.04 -1.84** |

**Table S7** Parameters of the best Ni K-edge EXAFS fitting results for $Ni_1$-N-C.

| Catalysts | shell | CN | R (Å) | $\sigma^2$ ($10^{-3}$Å$^2$) | ΔE (eV) | R factor | *K*-Range (Å$^{-1}$) | R-Range (Å) |
|---|---|---|---|---|---|---|---|---|
| **$Ni_1$-N-C** | **Ni-N** | **3.8** | **1.85** | **6.48** | **-3.664** | **0.00254** | **2.5 – 10.9** | **1.08 -2** |

**References**

(S1) B. H. R. Suryanto, H.-L. Du, D. Wang, J. Chen, A. N. Simonov and D. R. MacFarlane, *Nat. Catal.*, 2019, **2**, 290-296.

(S2) Z.-y. Gao, W.-j. Yang, X.-l. Ding, G. Lv and W.-p. Yan, *Phys. Chem. Chem. Phys.*, 2018, **20**, 7333-7341.

(S3) W. Yang, Z. Gao, X. Liu, X. Li, X. Ding and W. Yan, *Catal. Sci. Technol.*, 2018, **8**, 4159-4168.

(S4) J. K. Nørskov, J. Rossmeisl, A. Logadottir and L. Lindqvist, *J. Phys. Chem. B*, 2004, **108**, 17886-17892.

(S5) NIST Computational Chemistry Comparison and Benchmark Database. http://janaf.nist.gov/.

(S6) G. L. Long and J. D. Winefordner, *Anal. Chem.*, 1983, **55**, 712A-724A.